Ore Geology Reviews 101 (2018) 453–467

Contents lists available at ScienceDirect

Ore Geology Reviews

journal homepage: www.elsevier.com/locate/oregeorev

Constraints of hydrothermal and magmatic zircon on the origin of the Yaogangxian tungsten deposit, southern China

Xiang Wang[a,*], Minghua Ren[b]

[a] School of Earth Sciences and Engineering, Nanjing University, 210023 Nanjing, PR China
[b] Department of Geoscience, University of Nevada Las Vegas, Las Vegas, Nevada 89154-4010, USA

ARTICLE INFO

Keywords:
U–Pb dating
Wolframite-bearing quartz vein
Muscovite alkali-feldspar granite
Biotite monzogranite
Yaogangxian tungsten deposit

ABSTRACT

The Yaogangxian tungsten deposit, located in the central Nanling Range, is a well-known vein-type tungsten deposit and has been mined for centuries. This study focuses on the morphology, geochronology, and geochemistry of zircon crystals from wolframite-bearing quartz veins and coexisting alkali-feldspar granite to better understand the source of ore-forming materials and the exact timing of tungsten mineralization. All zircon grains, separated from the muscovite alkali-feldspar granite and the wolframite-bearing quartz veins, show core-to-rim structure. The overgrowth rims of the zircon grains from the muscovite alkali-feldspar granite and the wolframite-bearing quartz veins have crystallization ages of 133.4 ± 1.3 Ma and 133.7 ± 1.3 Ma, whereas the relict cores have ages of 155.3 ± 1.6 Ma and 154.8 ± 1.6 Ma, respectively. The ages of the cores are identical to the crystallization age of the hosting Yaogangxian biotite monzogranite. Thus, these cores were derived from the biotite monzogranite, whereas the overgrowth rims should have crystallized during the intrusion of muscovite alkali-feldspar granite and wolframite-bearing quartz veins. The geochemical consanguinity and similar ages of the muscovite alkali-feldspar granite and the ore veins suggest that they were both formed from the highly-fractionated granitic magma in an extensional setting. This highly-fractionated granitic melt might be extracted from the biotite-monzogranitic mush in a long surviving deep-seated magma chamber.

1. Introduction

Many tungsten deposits occur in the Nanling Range, South China (Xu et al., 2008; Zhao et al., 2017). The Yaogangxian tungsten deposit, located in the central Nanling Range, is a well-known vein-type tungsten deposit which has been mined for centuries. Wolframite-bearing quartz veins are hosted in both sedimentary country rocks and biotite monzogranite (Fig. 1). Those veins within Devonian sedimentary rocks extend downward and cut into the biotite monzogranite. The biotite monzogranite has a zircon U–Pb age of 155.4 Ma (Li et al., 2011a), which is consistent with most biotite monzogranites in the Nanling Range (150–160 Ma) (Hua et al., 2005; Li et al., 2007). However, the ore-forming age remains controversial, and ages obtained by multiple methods range from 153.0 to 175.8 Ma and concentrate between 153.0 and 156.0 Ma (Peng et al., 2006; Wang et al., 2008, 2009; Li et al., 2011b; Wang et al., 2012). The close spatial and temporal relationship between the ore veins and the biotite monzogranite (Liu, 1994; Pan and Cai, 2009; Wang et al., 2009; Guo et al., 2010; Chen et al., 2011; Li et al., 2015) is seemingly consistent with the most popular magmatic-hydrothermal model (e.g., Audétat et al., 2000; Pirajno, 2009). However, the model is challenged by two observations: (1) The ore-bearing quartz veins extend downward into the biotite monzogranite more than 1000 m (Fig. 2a) (Chen, 1981), indicating that these veins were much posterior to the biotite monzogranite; (2) The biotite monzogranite has no mineralogical and geochemical zonation except for changes of grain sizes from fine-grained in the margin to coarse-grained in the center (Zhang, 2012). This latter fact indicates that the biotite-monzogranitic magma experienced only a relatively short-time crystallization without crystal fractionation, which is necessary for the concentration and mobilization of the ore-forming materials (e.g., alkali, halogens, tungsten, and aqueous fluid).

Zircon grains from both the muscovite alkali-feldspar granite and the wolframite-bearing quartz veins were categorized based on their genetic characters in this study. The hydrothermal zircon grains from

* Corresponding author.
E-mail address: xwang@nju.edu.cn (X. Wang).

https://doi.org/10.1016/j.oregeorev.2018.07.011
Received 17 April 2018; Received in revised form 6 July 2018; Accepted 16 July 2018
Available online 30 July 2018
0169-1368/

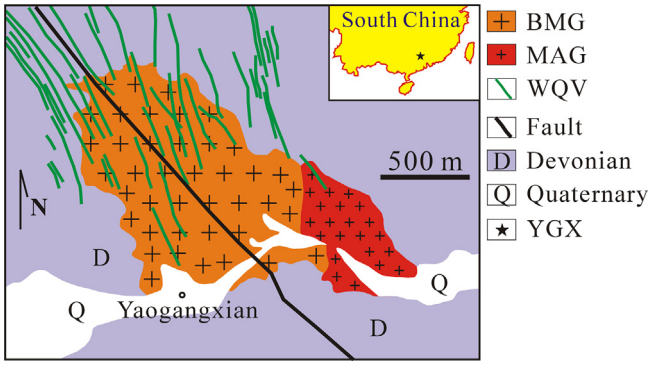

Fig. 1. Simplified geological map of the Yaogangxian granitic pluton in South China (after Huang, 2004; Li et al., 2011a). Abbreviations: BMG-Biotite monzogranite; MAG-Muscovite alkali-feldspar granite; WQV-Wolframite-bearing quartz vein; YGX-Location of the Yaogangxian tungsten deposit (marked by a solid star).

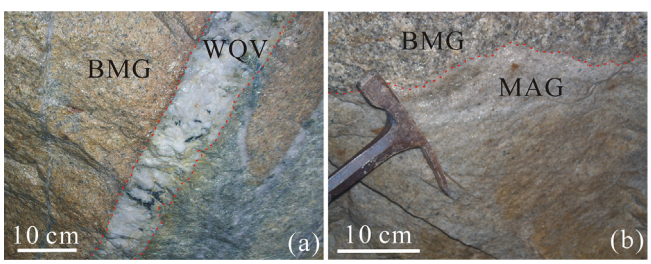

Fig. 2. Photographs of the contact between biotite monzogranite and wolframite-bearing quartz vein, and the contact between biotite monzogranite and muscovite alkali-feldspar granite in the Yaogangxian deposit. (a) The wolframite-bearing quartz vein (WQV) crosscuts the biotite monzogranite (BMG); (b) The muscovite alkali-feldspar granite (MAG) intrudes into the biotite monzogranite (BMG).

the ore veins, whose ages represent the time of tungsten mineralization, have been dated. The mineralization potential of the muscovite alkali-feldspar granite with reliable zircon U–Pb ages has been evaluated by comparing petrography and geochemistry between the muscovite alkali-feldspar granite and the biotite monzogranite. Combining geochemistry, mineralization, field observation, and the tectonic background, we here present the likely ore-forming process of the Yaogangxian tungsten deposit.

2. Geological background and analytical methods

The Yaogangxian tungsten deposit is located in the Nanling Range, South China. It is composed of large amount of the NNW–NWW-trending wolframite-bearing quartz veins, which intruded into Yaogangxian granitic pluton and Devonian sandstone, shale and limestone (Fig. 1). The Yaogangxian granitic pluton has an outcrop of 1.2 km^2, and consists of early-intruded medium–coarse-grained biotite monzogranite and late-intruded porphyritic fine-grained muscovite alkali-feldspar granite (Guo et al., 2010). This study has collected samples from both the wolframite-bearing quartz veins (Fig. 2a) and the muscovite alkali-feldspar granite (Fig. 2b) in the #67 mining shaft (at 113°18′59″ E, 25°38′38″ N) of the Yaogangxian deposit.

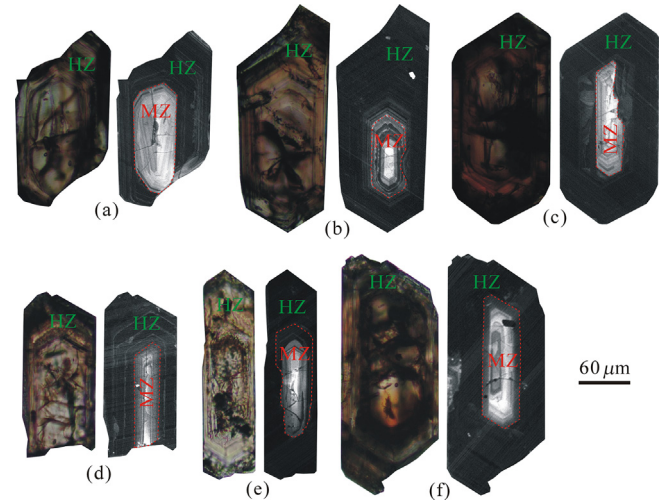

Fig. 3. Photomicrographs (transmitted light at left and CL at right for each grain) of zircon crystals (hydrothermal zircon-rim, magmatic zircon-core) from the muscovite alkali-feldspar granite (a–c) and the wolframite-bearing quartz veins (d–f) in the Yaogangxian tungsten deposit. Abbreviations: MZ-magmatic zircon; HZ-hydrothermal zircon.

These samples were processed with the standard mineral separation procedure, including crushing, pulverizing, and heavy mineral collecting by heavy liquid and magnetic separator. Only a small quantity of zircon grains, from both the muscovite alkali-feldspar granite and the wolframite-bearing quartz veins, can be collected from each 10 kg sample. The separates were mounted and polished to expose the center of zircon. The zircon shape and internal structure were studied by using optic microscope and cathodoluminescence detector. Trace elements and U–Pb and Lu–Hf isotope of zircon were collected with electron microprobe, *in-situ* laser ablation inductively-coupled plasma mass spectrometry (LA–ICPMS), and laser ablation multi-collector inductively coupled plasma mass spectrometry (LA–MC–ICPMS) in Nanjing University. Whole-rock major and trace elements of the muscovite alkali-feldspar granite have also been analyzed to study its genetic relationship with the tungsten mineralization.

3. Genetic characters of zircon

Zircon is an indispensable mineral which can provide prolific rock-forming information, such as material source, crystallization condition, crystallization time, etc. (Pupin, 1980; Rubin et al., 1989). Based on microscopic observation and microprobe analysis, zircon crystals from the muscovite alkali-feldspar granite and the wolframite-bearing quartz veins are basically possessing similar characters. The zircon crystals can be divided into two genetic groups: (1) the hydrothermal zircon, which crystallized from magmatic-hydrothermal fluid and occurred as overgrowth rim (right photographs in Fig. 3a–f), and (2) the magmatic zircon, which crystallized directly from granitic magma and occurred as relict core (right photographs in Fig. 3a–f).

Hydrothermal zircon from the muscovite alkali-feldspar granite and the wolframite-bearing quartz veins has following characters: (1) It is translucent with pale brown, murky brown, or orange red color (left photographs in Fig. 3a–f), and black in gray-scale CL image (right photographs in Fig. 3a–f); (2) It has combination of {1 1 0} prismatic

Table 1
Microprobe analyses (wt%) of hydrothemal zircon with relict zircon from the muscovite alkali-feldspar granite (YGX–2) and the wolframite-bearing quartz vein (YGX–6) in the Yaogangxian tungsten deposit.

Sample	Grain	Point	Phase	HfO_2	UO_2	ThO_2	P_2O_5	Others*	ZrO_2	SiO_2	Total
YGX–2	#101	#1	MZ	1.81	0.01	0.07	0.28	0.09	64.6	31.4	98.3
		#2	MZ	1.89	0.00	0.00	0.19	0.12	65.9	31.8	99.8
	#102	#3	MZ	1.84	0.00	0.02	0.10	0.01	65.1	31.7	98.7
	#104	#4	HZ	2.63	1.61	0.38	1.51	1.11	59.1	29.7	96.1
		#5	HZ	7.68	0.40	0.05	0.45	0.23	61.8	31.9	102.5
	#106	#6	HZ	4.35	2.24	0.21	0.99	2.45	55.6	28.1	93.9
		#7	HZ	3.92	2.46	0.24	0.77	3.29	53.4	27.4	91.5
	#107	#8	HZ	4.45	2.23	0.29	0.90	2.77	54.4	27.6	92.6
	#108	#9	MZ	1.63	0.00	0.12	0.14	0.00	64.9	31.8	98.6
		#10	MZ	1.74	0.00	0.00	0.17	0.03	65.7	31.9	99.6
		#11	HZ	2.90	0.47	0.08	0.11	0.00	63.1	31.7	98.3
		#12	HZ	4.31	1.71	0.13	0.80	0.70	60.4	30.6	98.6
	#109	#13	MZ	1.48	0.00	0.05	0.14	0.08	65.6	31.9	99.2
		#14	MZ	1.73	0.00	0.07	0.12	0.10	65.9	32.0	99.9
	#111	#15	HZ	4.93	1.46	0.14	0.98	0.52	60.2	30.8	98.9
	#113	#16	HZ	2.88	2.29	0.41	1.56	2.28	55.7	27.4	92.5
		#17	HZ	4.39	1.31	0.15	0.52	0.16	61.7	31.0	99.2
	#114	#18	MZ	1.93	0.00	0.07	0.01	0.07	64.4	32.0	98.4
		#19	HZ	3.27	1.40	0.14	0.52	0.29	61.5	31.1	98.2
		#20	HZ	3.54	1.43	0.18	0.47	0.67	60.7	30.0	97.0
	#203	#1	MZ	1.53	0.00	0.03	0.03	0.10	64.1	31.8	97.6
		#2	MZ	1.43	0.00	0.06	0.09	0.08	65.0	31.8	98.5
	#204	#3	MZ	1.68	0.00	0.00	0.11	0.14	63.9	31.7	97.5
		#4	HZ	2.62	0.50	0.10	0.14	0.14	63.6	31.5	98.5
	#205	#5	HZ	2.54	0.78	0.19	0.17	0.20	64.3	31.7	99.9
	#206	#6	HZ	2.85	1.49	0.07	0.39	0.34	60.8	30.4	96.3
	#208	#7	HZ	3.16	0.28	0.05	0.26	0.05	62.3	31.6	97.7
		#8	HZ	3.18	0.41	0.06	0.22	0.03	64.3	32.0	100.2
	#211	#9	HZ	2.63	0.83	0.25	0.13	0.09	63.5	31.7	99.2
	#212	#10	MZ	1.63	0.04	0.19	0.20	0.05	64.6	31.6	98.3
		#11	HZ	3.35	1.24	0.17	0.36	0.15	61.0	30.8	97.1
		#12	HZ	2.68	2.24	0.35	0.41	0.32	59.7	30.0	95.6
	#214	#13	HZ	3.49	1.11	0.12	0.17	0.11	62.5	31.4	98.9
	#215	#14	HZ	2.40	0.35	0.16	0.16	0.06	63.3	31.4	97.8
		#15	HZ	5.81	0.54	0.01	0.34	0.05	62.7	31.6	101.0
	#217	#16	HZ	2.66	0.49	0.10	0.20	0.00	64.4	31.8	99.6
		#17	HZ	2.44	0.29	0.12	0.15	0.07	63.1	31.5	97.7
	#218	#18	HZ	2.66	0.64	0.09	0.14	0.12	62.9	31.7	98.2
	#219	#19	HZ	3.08	1.54	0.34	0.65	0.71	60.6	29.8	96.8
	#221	#20	MZ	1.71	0.00	0.00	0.05	0.06	65.3	31.9	98.9
		#21	HZ	2.70	0.48	0.13	0.29	0.19	64.2	31.4	99.4
	#222	#22	HZ	3.59	0.11	0.05	0.12	0.28	65.1	32.0	101.2
	#224	#23	HZ	2.30	0.21	0.12	0.10	0.13	64.0	32.0	98.8
	#308	#24	HZ	2.88	1.29	0.17	0.19	0.09	61.5	31.3	97.4
	#310	#25	HZ	5.06	1.13	0.30	0.88	0.13	57.3	29.7	94.5
	#315	#26	MZ	1.84	0.00	0.11	0.02	0.04	64.2	31.6	97.8
		#27	HZ	2.39	0.62	0.29	0.17	0.04	62.7	31.5	97.8
	#317	#28	HZ	2.66	2.76	0.39	0.68	1.97	54.3	27.6	90.3
	#325	#29	HZ	2.16	0.52	0.18	0.19	0.06	63.5	31.7	98.3
		#30	MZ	1.44	0.00	0.06	0.10	0.05	64.5	32.1	98.2
		#31	HZ	2.31	0.31	0.10	0.21	0.04	65.1	31.8	99.8
	#333	#32	HZ	2.29	2.00	0.45	0.29	0.34	60.0	30.4	95.8
YGX–6	#110	#1	HZ	2.08	2.47	0.65	1.09	3.07	53.2	25.9	88.5
		#2	HZ	2.83	1.04	0.07	0.00	0.07	62.7	31.0	97.7
	#114	#3	MZ	1.70	0.00	0.01	0.00	0.07	65.3	31.6	98.7
	#116	#4	MZ	1.35	0.00	0.00	0.00	0.08	66.1	32.1	99.6
		#5	MZ	1.57	0.00	0.02	0.00	0.05	65.0	31.7	98.3
		#6	MZ	1.62	0.00	0.00	0.00	0.13	65.4	31.7	98.8
	#117	#7	MZ	1.81	0.00	0.01	0.00	0.08	65.2	31.8	99.0
		#8	MZ	1.47	0.00	0.00	0.00	0.11	66.5	31.9	100.0
		#9	MZ	1.70	0.00	0.00	0.00	0.14	65.6	31.9	99.3
	#119	#10	MZ	1.45	0.00	0.00	0.00	0.07	65.6	31.6	98.7
		#11	MZ	1.40	0.00	0.02	0.00	0.09	65.5	31.5	98.6
		#12	MZ	1.38	0.00	0.00	0.00	0.08	65.5	31.5	98.5
	#120	#13	MZ	1.39	0.00	0.00	0.00	0.09	65.9	31.6	98.9
		#14	MZ	1.63	0.00	0.01	0.00	0.05	64.4	31.4	97.5
	#121	#15	HZ	2.72	0.02	0.00	0.00	0.05	64.9	31.6	99.3
	#122	#16	MZ	1.70	0.00	0.00	0.00	0.06	65.3	31.7	98.8
	#123	#17	MZ	1.27	0.00	0.00	0.00	0.06	65.4	31.4	98.2
		#18	MZ	1.66	0.00	0.00	0.00	0.09	64.4	31.1	97.3
	#124	#19	MZ	1.51	0.00	0.00	0.00	0.06	64.4	31.3	97.3
	#125	#20	HZ	2.35	2.77	0.22	1.54	5.29	44.4	24.5	81.1

(*continued on next page*)

Table 1 (*continued*)

Sample	Grain	Point	Phase	HfO_2	UO_2	ThO_2	P_2O_5	Others*	ZrO_2	SiO_2	Total
		#21	HZ	2.08	3.96	0.48	1.82	3.50	48.7	25.1	85.7
	#126	#22	MZ	1.32	0.00	0.00	0.00	0.07	65.4	31.9	98.7
	#202	#1	HZ	4.90	2.60	0.15	0.79	1.78	54.1	28.2	92.5
		#2	MZ	1.64	0.00	0.00	0.00	0.10	64.8	31.5	98.0
	#203	#3	HZ	3.18	1.49	0.04	0.14	0.10	60.3	30.1	95.3
		#4	HZ	2.40	1.11	0.17	0.00	0.10	62.7	31.1	97.6
	#205	#5	HZ	2.11	7.04	0.72	0.56	1.70	52.9	27.7	92.7
		#6	MZ	1.45	0.00	0.09	0.00	0.07	65.1	31.4	98.1
	#206	#7	MZ	1.45	0.00	0.00	0.00	0.11	65.8	31.6	98.9
		#8	HZ	2.51	0.27	0.06	0.00	0.12	63.5	31.1	97.5
	#207	#9	HZ	2.30	0.50	0.13	0.00	0.04	62.9	31.1	97.0
		#10	MZ	1.46	0.00	0.00	0.00	0.07	65.6	31.7	98.8
	#211	#11	MZ	1.70	0.00	0.00	0.00	0.06	65.3	31.6	98.6
		#12	MZ	1.85	0.00	0.00	0.00	0.06	65.2	31.7	98.8
		#13	MZ	1.77	0.00	0.00	0.00	0.13	66.0	31.9	99.8
	#213	#14	MZ	1.51	0.00	0.00	0.00	0.07	65.7	31.8	99.1
		#15	HZ	5.12	0.43	0.00	0.00	0.05	61.8	31.4	98.8
	#216	#16	MZ	1.66	0.00	0.00	0.00	0.06	65.5	31.6	98.7
		#17	MZ	1.90	0.35	0.08	0.00	0.06	64.4	31.7	98.5
	#217	#18	MZ	1.62	0.00	0.00	0.00	0.05	65.5	31.8	99.0
		#19	MZ	1.98	0.06	0.00	0.00	0.14	65.5	32.0	99.7
	#218	#20	MZ	1.34	0.00	0.00	0.00	0.20	65.5	31.8	98.9
		#21	MZ	1.86	0.00	0.00	0.00	0.07	65.3	31.7	98.9
	#219	#22	MZ	1.49	0.00	0.00	0.00	0.06	66.0	32.1	99.6
		#23	HZ	3.77	0.23	0.23	0.02	0.57	53.6	27.4	85.8
		#24	HZ	2.91	1.14	0.02	0.00	0.10	62.3	31.3	97.8
	#221	#25	HZ	3.59	0.73	0.00	0.30	0.28	60.2	30.1	95.2
		#26	HZ	4.43	0.68	0.00	0.04	0.08	62.4	31.4	99.1
		#27	HZ	3.97	0.65	0.00	0.00	0.11	62.3	30.5	97.6
	#226	#28	MZ	1.42	0.00	0.00	0.00	0.11	65.9	32.1	99.6
		#29	MZ	1.39	0.00	0.00	0.00	0.11	65.7	32.1	99.3
		#30	MZ	1.86	0.03	0.00	0.00	0.08	64.6	31.5	98.0
	#230	#31	MZ	1.67	0.00	0.00	0.00	0.08	65.2	31.5	98.5
	#233	#32	HZ	3.79	0.44	0.00	0.00	0.02	61.6	30.8	96.6

*Others mainly include contents of Y_2O_3, Ce_2O_3, Al_2O_3, La_2O_3, MnO, WO_3.

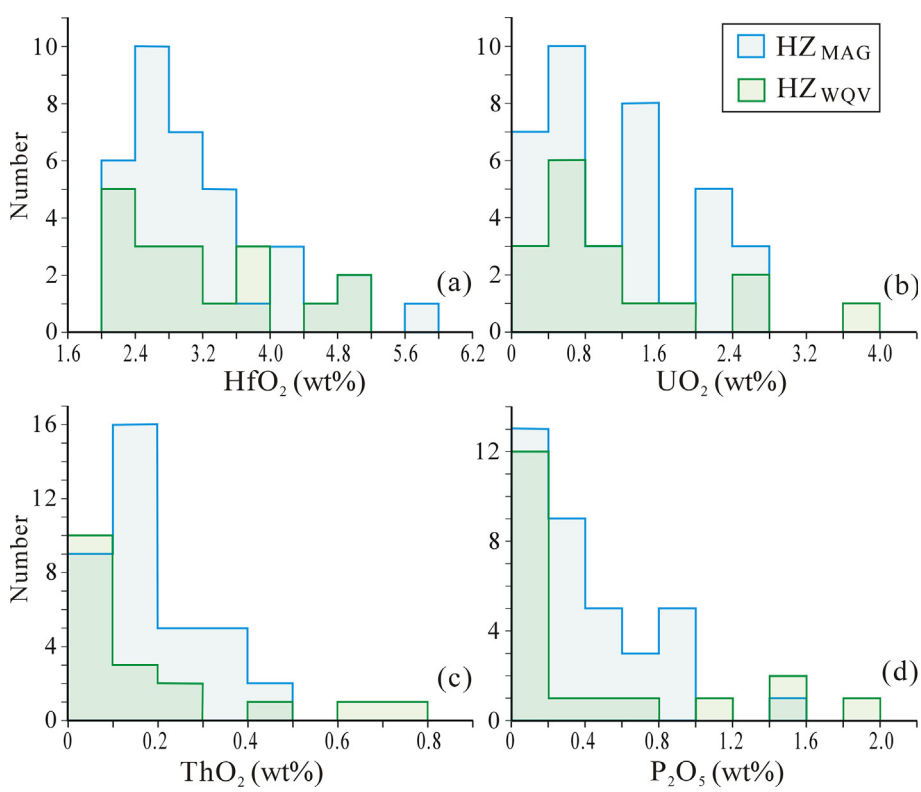

Fig. 4. Histograms of the minor elements of the hydrothermal zircon form the muscovite alkali-feldspar granite (HZ_{MAG}) and the wolframite-bearing quartz veins (HZ_{WQV}) in the Yaogangxian tungsten deposit (data from Table 1): (a) HfO_2 (wt%), (b) UO_2 (wt%), (c) ThO_2 (wt%), (d) P_2O_5 (wt%).

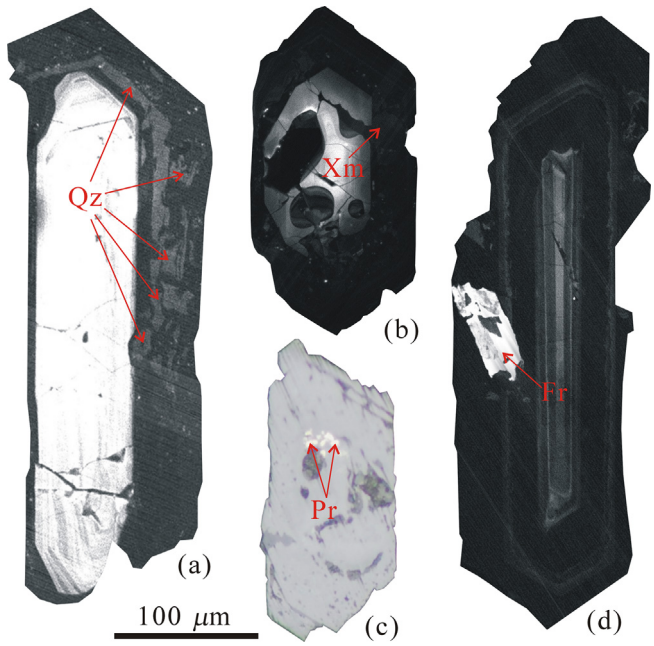

Fig. 5. Inclusions within the hydrothermal zircon: (a) CL image showing quartz within the hydrothermal zircon from the wolframite-bearing quartz veins; (b) CL image showing xenotime within the hydrothermal zircon from the wolframite-bearing quartz veins; (c) reflected light image showing pyrite within the hydrothermal zircon from the wolframite-bearing quartz veins; (d) CL image showing fluorite within the hydrothermal zircon the muscovite alkali-feldspar granite. Abbreviations: Qz-quartz; Xm-xenotime; Pr-pyrite; Fr-fluorite.

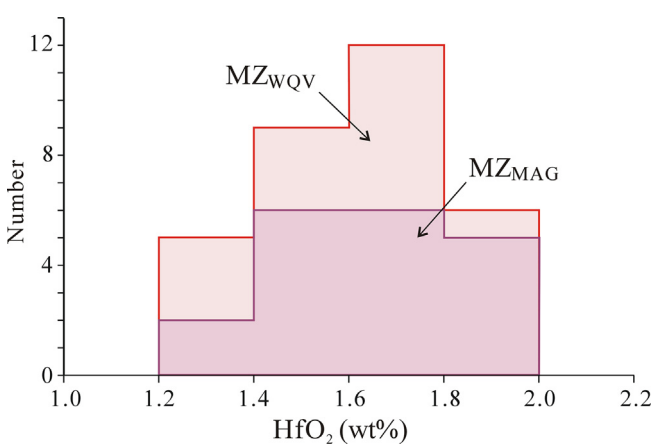

Fig. 6. Histograms of HfO_2 (wt%) of the magmatic zircon from the muscovite alkali-feldspar granite (MZ_{MAG}) and the wolframite-bearing quartz veins (MZ_{WQV}) in the Yaogangxian tungsten deposit (data from Table 1).

faces and {1 0 1} pyramidal faces (left photographs in Fig. 3a–f); (3) EMP analysis (Table 1) shows that it is extremely enriched in Hf (from 2.08 to 7.68 wt% HfO_2, Fig. 4a), U (0.02 to 7.04 wt% UO_2, Fig. 4b), Th (from 0 to 0.72 wt% ThO_2, Fig. 4c), and P (from 0 to 1.82 wt% P_2O_5, Fig. 4d); (4) It contains hydrothermal mineral (quartz, Fig. 5a; and fluorite, Fig. 5d) and ore mineral (xenotime, Fig. 5b; and pyrite, Fig. 5c) inclusions. These features have been reported in the literatures as the distinguishing characteristics of the hydrothermal zircon (Claoué-Long et al., 1990; Kerrich and King, 1993; Rubin et al., 1993; Hoskin, 2005; Pelleter et al., 2007; Zhao et al., 2016).

Magmatic zircon from the muscovite alkali-feldspar granite and the wolframite-bearing quartz veins has following characters: (1) It is colorless and transparent, with presence of {2 1 1} pyramidal faces (right photo in Fig. 3a); (2) It shows bright and oscillatory zoning and sector zoning in the CL images (right photos in Fig. 3a–f); (3) EMP analysis (Table 1) shows that it contains regular Hf contents (from 1.27 to 1.98 wt% HfO_2, Fig. 6) and low U (mean 0.01 wt% UO_2), Th (mean 0.02 wt% ThO_2) and P (mean 0.03 wt% P_2O_5) contents (generally below the electron-microprobe detection limits). These trace element characters reflect that the zircon crystallized from the granitic melt under equilibrium condition (Wang et al., 2010, 2011); (4) It contains abundant apatite (left photo in Fig. 3f) and melt inclusions (left photo in Fig. 3a). These are the common features for the zircon crystallized from the granitic magma (Pupin, 1980; Wang et al., 2007).

4. Geochronology

Zircon U–Pb ages of the muscovite alkali-feldspar granite and the wolframite-bearing quartz veins in the Yaogangxian deposit are listed in Table 2. The zircon U–Pb data indicate that there was more or less Pb loss due to certain metamictization of the zircon grains from the studied rocks.

The U–Pb isotopes of the zircon rims (i.e., hydrothermal zircon) from the muscovite alkali-feldspar granite (YGX–2) yield a lower intercept age of 133.4 ± 1.3 Ma (n = 16, MSWD = 0.15, Fig. 7a), and U–Pb isotopes of the zircon cores (i.e., magmatic zircon) yield a concordant age of 155.3 ± 1.6 Ma (n = 10, MSWD = 0.28, Fig. 7a), respectively. The crystallization age of the hydrothermal zircon represents the emplacement time of the muscovite alkali-feldspar granite and is significantly different from the previously-reported age of the Yaogangxian muscovite alkali-feldspar granite (157.6 Ma, Li et al., 2011a). The crystallization age of the relict zircon is similar to that of magmatic zircon from the Yaogangxian biotite monzogranite (155.4 Ma, Li et al., 2011a).

The zircon U–Pb isotopes from the wolframite-bearing quartz vein (YGX–6) yield two concordant ages: (1) 133.7 ± 1.3 Ma (n = 12, MSWD = 0.32, Fig. 7b) for the zircon rims (i.e., hydrothermal zircon), and (2) 154.8 ± 1.6 Ma (n = 12, MSWD = 0.64, Fig. 7b) for the zircon cores (i.e., magmatic zircon). As the hydrothermal mineral from the wolframite-bearing quartz veins, the zircon rim is always crystallizing together with the ore minerals and can contain some ore mineral inclusions (see Section 3). Thus, the zircon rim should be congenetic with the wolframite (see Section 5.3). Consequently, the Yaogangxian tungsten deposit should form at 133.7 ± 1.3 Ma based on our new zircon age, although it is significantly different from the previously-reported ages of the wolframite-bearing quartz veins (175.8–153.0 Ma, Peng et al., 2006; Wang et al., 2008; Wang et al., 2009, 2012; Li et al., 2011b). The weighted average age of relict zircon also is similar to that of magmatic zircon from the Yaogangxian biotite monzogranite (155.4 Ma, Li et al., 2011a).

5. Discussion

The mineralization age is one of the most crucial factors in determining the potential sources of ore deposit and the correlated

Table 2
Data from LA–ICPMS dating of hydrothermal zircons (HZ) and magmatic zircons (MZ) from the muscovite alkali-feldspar granite (YGX–2) and the wolframite-bearing quartz vein (YGX–6) in the Yaogangxian tungsten deposit.

Sample	Grain	Phase	Radiogenetic ratios						Apparent ages (Ma)					
	–Spot		$^{206}Pb/^{238}U$	± 1σ	$^{207}Pb/^{235}U$	± 1σ	$^{207}Pb/^{206}Pb$	± 1σ	$^{206}Pb/^{238}U$	± 1σ	$^{207}Pb/^{235}U$	± 1σ	$^{207}Pb/^{206}Pb$	± 1σ
YGX–2	104–1	HZ	0.02171	0.00031	0.26310	0.00524	0.08793	0.00184	138.5	2.0	237.2	4.2	1381.0	39.6
	107–1	HZ	0.02141	0.00031	0.24047	0.00537	0.08148	0.00194	136.6	2.0	218.8	4.4	1233.1	45.7
	108–2	MZ	0.02446	0.00038	0.16625	0.00594	0.04931	0.00181	155.8	2.4	156.2	5.2	162.5	83.8
	109–3	MZ	0.02457	0.00051	0.16741	0.01067	0.04941	0.00326	156.5	3.2	157.2	9.3	167.4	147.4
	111–1	HZ	0.02105	0.00026	0.15849	0.00206	0.05466	0.00073	134.3	1.6	149.4	1.8	398.4	29.5
	113–2	HZ	0.02118	0.00029	0.17588	0.00289	0.06041	0.00103	135.1	1.8	164.5	2.5	618.2	36.2
	113–4	HZ	0.02087	0.00025	0.14676	0.00282	0.05105	0.00105	133.2	1.6	139.0	2.5	243.1	46.6
	113–5	MZ	0.02461	0.00039	0.17864	0.00674	0.05272	0.00209	156.7	2.5	166.9	5.8	316.9	87.7
	113–6	MZ	0.02443	0.00032	0.18514	0.00374	0.05505	0.00114	155.6	2.0	172.5	3.2	414.0	44.9
	114–1	HZ	0.02203	0.00026	0.32115	0.00578	0.10581	0.00203	140.5	1.7	282.8	4.4	1728.5	34.8
	114–4	HZ	0.02086	0.00038	0.13962	0.00407	0.04867	0.00148	133.1	2.4	132.7	3.6	131.8	70.0
	203–1	MZ	0.02429	0.00050	0.16701	0.01241	0.04998	0.00379	154.7	3.1	156.8	10.8	193.8	167.3
	203–2	MZ	0.02421	0.00042	0.16415	0.00906	0.04923	0.00278	154.2	2.6	154.3	7.9	158.6	127.0
	203–3	MZ	0.02404	0.00040	0.16281	0.00712	0.04919	0.00221	153.1	2.5	153.2	6.2	156.7	102.0
	204–1	HZ	0.02125	0.00033	0.18592	0.00437	0.06356	0.00155	135.5	2.1	173.1	3.7	726.9	51.0
	204–2	HZ	0.02091	0.00029	0.16548	0.00256	0.05749	0.00092	133.4	1.8	155.5	2.2	509.8	35.0
	204–3	HZ	0.02109	0.00028	0.16985	0.00239	0.05848	0.00084	134.5	1.8	159.3	2.1	547.6	31.2
	206–1	MZ	0.02423	0.00035	0.16269	0.00540	0.04873	0.00168	154.4	2.2	153.1	4.7	134.7	79.1
	206–2	MZ	0.02425	0.00034	0.18309	0.00547	0.05479	0.00171	154.5	2.1	170.7	4.7	403.7	67.5
	208–1	HZ	0.02189	0.00031	0.32383	0.00582	0.10741	0.00201	139.6	2.0	284.8	4.5	1755.9	33.8
	208–2	HZ	0.02125	0.00030	0.15414	0.00268	0.05267	0.00095	135.6	1.9	145.6	2.4	314.4	40.4
	208–3	HZ	0.02112	0.00029	0.20463	0.00519	0.07032	0.00189	134.7	1.8	189.0	4.4	937.9	54.1
	214–1	HZ	0.02101	0.00032	0.15263	0.00327	0.05274	0.00119	134.0	2.0	144.2	2.9	317.7	50.4
	218–1	HZ	0.02120	0.00038	0.19543	0.00734	0.06689	0.00263	135.2	2.4	181.3	6.2	834.4	79.9
	221–1	MZ	0.02465	0.00033	0.18863	0.00394	0.05550	0.00121	157.0	2.1	175.5	3.4	432.1	47.3
	224–1	HZ	0.02158	0.00033	0.26616	0.00593	0.08951	0.00211	137.6	2.1	239.6	4.8	1415.0	44.3
YGX–6	110–1	HZ	0.02080	0.00038	0.14621	0.00515	0.05102	0.00183	132.7	2.4	138.6	4.6	241.5	80.4
	114–1	MZ	0.02418	0.00040	0.16491	0.00769	0.04947	0.00236	154.0	2.5	155.0	6.7	170.2	107.9
	114–2	HZ	0.02107	0.00036	0.14217	0.00399	0.04895	0.00132	134.4	2.3	135.0	3.6	145.5	62.1
	114–3	HZ	0.02107	0.00040	0.14178	0.00541	0.04881	0.00188	134.4	2.5	134.6	4.8	138.5	88.2
	116–1	MZ	0.02394	0.00050	0.16491	0.00905	0.04997	0.00285	152.5	3.2	155.0	7.9	193.5	127.4
	116–2	MZ	0.02387	0.00033	0.16603	0.00457	0.05045	0.00141	152.1	2.1	156.0	4.0	215.8	63.3
	117–1	MZ	0.02459	0.00046	0.16811	0.00719	0.04958	0.00217	156.6	2.9	157.8	6.3	175.2	99.2
	119–1	MZ	0.02443	0.00043	0.16535	0.00672	0.04910	0.00205	155.6	2.7	155.4	5.9	152.5	94.8
	120–1	HZ	0.02119	0.00045	0.14331	0.00692	0.04906	0.00243	135.2	2.8	136.0	6.2	150.7	112.0
	120–2	MZ	0.02514	0.00053	0.17071	0.00962	0.04926	0.00288	160.0	3.3	160.0	8.3	160.1	131.5
	124–1	MZ	0.02456	0.00037	0.16657	0.00486	0.04919	0.00145	156.4	2.3	156.4	4.2	157.1	67.5
	126–1	MZ	0.02406	0.00051	0.16285	0.00954	0.04909	0.00294	153.3	3.2	153.2	8.3	151.9	134.7
	202–2	MZ	0.02388	0.00047	0.16338	0.00946	0.04963	0.00296	152.2	2.9	153.7	8.3	177.5	133.5
	202–3	HZ	0.02118	0.00028	0.14235	0.00318	0.04875	0.00110	135.1	1.8	135.1	2.8	135.7	52.0
	202–4	HZ	0.02087	0.00028	0.14289	0.00359	0.04968	0.00127	133.2	1.8	135.6	3.2	179.8	58.6
	203–3	HZ	0.02085	0.00026	0.14525	0.00319	0.05054	0.00114	133.0	1.7	137.7	2.8	219.9	51.2
	203–4	HZ	0.02117	0.00041	0.14615	0.00691	0.05011	0.00247	135.1	2.6	138.5	6.1	200.2	110.4
	208–1	HZ	0.02053	0.00037	0.14406	0.00570	0.05086	0.00204	131.0	2.3	136.7	5.1	234.6	90.1
	213–1	MZ	0.02447	0.00049	0.16534	0.00965	0.04901	0.00294	155.9	3.1	155.4	8.4	148.5	135.1
	215–1	HZ	0.02072	0.00049	0.14352	0.00848	0.05026	0.00305	132.2	3.1	136.2	7.5	207.1	135.0
	222–1	MZ	0.02437	0.00047	0.16520	0.00834	0.04918	0.00252	155.2	3.0	155.2	7.3	156.4	115.9
	222–2	HZ	0.02103	0.00032	0.14492	0.00322	0.04999	0.00104	134.2	2.0	137.4	2.9	194.6	47.6
	226–1	MZ	0.02444	0.00042	0.16637	0.00699	0.04937	0.00213	155.7	2.6	156.3	6.1	165.6	97.6
	231–2	HZ	0.02084	0.00047	0.14638	0.00748	0.05103	0.00253	132.9	3.0	138.7	6.6	242.3	110.4

tectonic environment of the ore-forming process. Based on the age of hydrothermal zircon from the wolframite-bearing quartz veins, the Yaogangxian tungsten deposit should form at 133.7 Ma. This age is distinctly different from the previously-reported ore ages (ranging from 175.8 Ma to 153.0 Ma, Wang et al., 2008, 2009, 2012; Peng et al., 2006; Li et al., 2011b). In the following sections, we are going to discuss the possible rationales of the contretemps between the previous works and ours.

5.1. Parental rock

Based on close spatial and temporal relationship between the biotite monzogranite and the wolframite-bearing quartz veins in the Yaogangxian deposit, the biotite monzogranite has been considered as the source of the tungsten mineralization by many researchers (Liu, 1994; Pan and Cai, 2009; Wang et al., 2009; Guo et al., 2010; Chen et al., 2011; Li et al., 2015). However, our work indicates that the

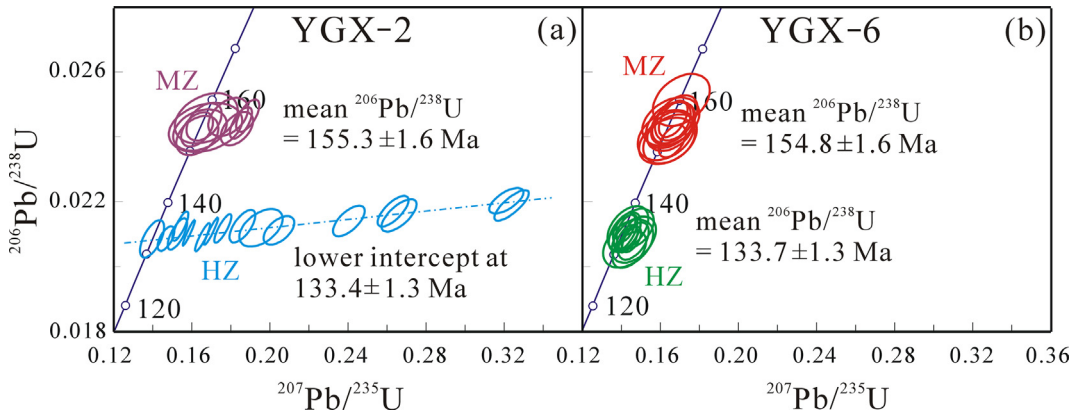

Fig. 7. U–Pb Concordia diagrams of LA–ICPMS analyses for the hydrothermal zircon (HZ) and the magmatic zircon (MZ) from muscovite alkali-feldspar granite (a: YGX–2) and wolframite-bearing quartz veins (b: YGX–6) in the Yaogangxian tungsten deposit (data from Table 2).

Yaogangxian tungsten mineralization should be correlated with the muscovite alkali-feldspar granite. This interpretation is based on three observations as follows: (1) presence of highly-differentiated muscovite alkali-feldspar granite; (2) compositional consanguinity between muscovite alkali-feldspar granite and ore vein; and (3) similarity in crystallization age between muscovite alkali-feldspar granite and ore vein.

– Muscovite alkali-feldspar granite from highly-differentiated magma

The muscovite alkali-feldspar granite is geochemically characterized with three features: (1) Major element data (Table 3) show that it is enriched in Si (ranging from 74.44 to 76.86 wt% SiO_2, Fig. 8a), and depleted in Ca (ranging from 0.49 to 0.93 wt% CaO, Fig. 8a), Mg (ranging from 0.04 to 0.06 wt% MgO, Fig. 8b), Fe (ranging from 0.47 to 1.21 wt% FeO^T, Fig. 8b), Ti (ranging from 0.01 to 0.04 wt% TiO_2, Fig. 8b) and P (ranging from 0.01 to 0.06 wt% P_2O_5, Fig. 8b) relative to the biotite monzogranite. (2) Trace element data (Table 4) show that it is depleted in compatible elements (Ba, Co, Cr, Hf, Ni, Sr, V, Zr) and enriched in incompatible elements (Be, Cs, Li, Nb, Pb, Rb, Sn, Ta, Th, U, W, Y) relative to the biotite monzogranite or the upper crust (Fig. 9a). (3) Rare earth element data (Table 5) show that it is depleted in LREE (ranging from 26.5 to 50.8 ppm) and enriched in HREE (ranging from 23.8 to 76.7 ppm) relative to the biotite monzogranite. The chondrite-normalized REE values of the muscovite alkali-feldspar granite show a near flat pattern with large negative Eu anomaly (average Eu/Eu∗ = 0.03, see Table 5) (Fig. 9b). These three features are generally correlated with highly-differentiated granitic magma through the enduring fractional crystallization of high-melting-point minerals (such as Fe–Ti oxides, zircon, apatite, pyroxene, amphibole, biotite, and Ca-plagioclase) (Černý et al., 2005; Thomas et al., 2005).

– Compositional consanguinity between muscovite alkali-feldspar granite and ore vein

Because of the consumption of the zircon grains by laser ablation during the *in-situ* U–Pb dating, only eight spots of Hf isotope ratios have been obtained (Table 6). The initial $^{176}Hf/^{177}Hf$ ratios of the hydrothermal zircon vary from 0.282128 to 0.282404 in the muscovite alkali-feldspar granite, and 0.282123 to 0.282347 in the wolframite-bearing quartz veins, respectively. Based on crystallization ages presented in Table 2, the $\varepsilon_{Hf}(t)$ values were calculated (Table 6). It can be observed that the hydrothermal zircon from the muscovite alkali-feldspar granite and the wolframite-bearing quartz veins in the Yaogangxian deposit shows similar variations in their $\varepsilon_{Hf}(t)$ values (Fig. 10). This is one of the key evidences that the hydrothermal zircon from the wolframite-bearing quartz veins and the muscovite alkali-feldspar granite has compositional consanguinity.

– Similarity in crystallization age between muscovite alkali-feldspar granite and ore vein

The most crucial point is that the crystallization ages of the hydrothermal zircon from both the muscovite alkali-feldspar granite (133.4 ± 1.3 Ma) and the wolframite-bearing quartz veins (133.7 ± 1.3 Ma) are almost identical. The muscovite alkali-feldspar granites from the Qianlishan and Qitianling plutons, near the Yaogangxian pluton, also give ages of 136–137 Ma (Mao et al., 1998) and 140 Ma (Li et al., 2006), respectively. The mineralization ages of the Shizhuyuan tungsten deposit and the Furong tin deposit are 134.0 Ma (Mica Ar–Ar, Mao et al., 2004), 133.0 Ma (ore Sm–Nd, Li et al., 2006), and 136.0 (ore Rb–Sr, Wang et al., 2003), respectively. As for the previously-reported zircon U–Pb age of 157.6 Ma from the Yaogangxian muscovite alkali-feldspar granite (Li et al., 2011a), the U–Pb isotopes might be collected from the zircon cores (e.g., the magmatic relict zircon), which dated as 155.3 Ma in this work. It is difficult for us to evaluate the previously-reported 157.6 Ma age without further information from those researchers.

The close association of the tungsten deposit with the muscovite alkali-feldspar granite has also been observed in many other places, such as Limousin, France (Lerouge et al., 2007), New South Wales, Australia (Audétat et al., 2000), Transbaikalia, Russia (Badanina et al., 2004), Great Basin, USA (Barton, 1987), Choquene District, Peru (Farrar et al., 1990), Erzgebirge, Germany (Forster et al., 1999), Central Kazakhstan (Heinhorst and Lehmann, 1995), Newfoundland, Canada (Higgins, 1985), San Finx and the Virgen de la Encina, Spain (Mangas and Perez-Torrado, 1995), and Phuket, Thailand (Suwimonprecha et al., 1995). Consequently, the muscovite alkali-feldspar granite could be the provider of ore-forming material for the Yaogangxian tungsten deposit.

Table 3
Major oxide concentrations (wt%) of biotite monzogranites and muscovite alkali-feldspar granites in the Yaogangxian pluton and its neighboring area.

Rock	Biotite monzogranite														Muscovite alkali-feldspar granite						
Sample	c–10a	c–10b	c–10d	c–10e	c–12	c–15	c–16	c–17	c–18	c–22a	c–26	c–27a	c–27b	c–27c	19–3	21–8	YGX–34	YGX–36	YGX–37	YGX–2	YGX–3
SiO_2	67.03	67.67	69.59	67.97	66.48	69.08	68.19	69.59	67.63	70.55	72.41	66.14	65.95	67.25	71.92	75.78	75.78	76.78	74.44	76.86	75.91
TiO_2	0.58	0.60	0.48	0.78	0.72	0.58	0.64	0.66	0.58	0.45	0.45	0.69	0.94	0.81	0.11	0.04	0.01	0.01	0.01	0.02	0.04
Al_2O_3	14.27	14.51	12.96	14.19	14.33	13.57	13.85	13.15	13.47	13.88	13.36	14.81	13.77	14.03	13.46	12.80	12.89	12.65	13.44	12.57	12.95
FeO^T	4.26	3.91	3.19	4.61	4.45	3.81	3.89	4.10	3.97	3.05	3.05	3.95	5.43	4.55	2.62	1.21	0.64	0.56	0.75	0.47	0.76
MnO	0.06	0.07	0.06	0.08	0.07	0.05	0.07	0.08	0.07	0.05	0.05	0.07	0.09	0.08	0.53	0.13	0.13	0.11	0.10	0.04	0.10
MgO	0.72	0.76	0.58	0.90	0.85	0.72	0.75	0.79	0.56	0.52	0.43	0.86	1.21	0.95	0.35	0.05	0.06	0.04	0.06	0.04	0.06
CaO	1.85	1.88	1.60	2.84	2.50	2.46	2.35	2.75	2.26	2.02	1.83	2.34	2.81	2.81	1.87	0.72	0.74	0.52	0.93	0.49	0.69
Na_2O	3.14	3.00	2.77	3.30	3.42	3.31	3.12	3.21	2.99	3.15	3.22	3.21	3.07	2.99	0.01	4.24	3.91	3.36	3.14	3.92	3.34
K_2O	5.35	6.18	5.63	4.28	4.77	4.98	5.52	4.43	5.56	5.08	4.99	5.83	4.84	4.17	5.90	4.14	4.38	4.35	5.35	4.53	4.77
P_2O_5	0.19	0.23	0.16	0.26	0.24	0.21	0.21	0.22	0.21	0.12	0.11	0.21	0.28	0.26	0.03	0.01	0.04	0.04	0.06	0.04	0.03
LOI	1.67	1.18	1.69	1.13	1.02	1.19	0.74	1.02	2.96	0.84	0.74	1.54	1.27	1.26	2.34	0.45	0.77	1.04	1.13	0.75	1.08
Total	99.59	100.42	99.06	100.85	99.35	100.38	99.76	100.46	100.70	100.05	100.98	100.09	100.26	99.67	99.31	99.57	99.34	99.47	99.43	99.78	99.81

Note: FeO^T—All Fe is calculated as FeO. Data source: Samples c–10a, c–10b, c–10d, c–12, c–15, c–16, c–17, c–18, c–22a, c–26, c–27a, c–27b, c–27c from the Qitianling pluton (Deng et al., 2005); Samples 19–3 and 21–8 from the Yaogangxian pluton (Wang, 2008); Samples YGX–34, YGX–36 and YGX–37 from the Yaogangxian pluton (Xie et al., 2013); Samples YGX–2 and YGX–3 from the Yaogangxian pluton (this study).

5.2. Tectonic constraints

Many metallogenic studies show that most of metal mineralization occur in extensional tectonic settings (Groves and Bierlein, 2007; Bastos Neto et al., 2009; Zhao et al., 2017), where large-scale fractures and faults in the upper continental crust can serve as the pathway to transport the ore-forming material and also provided the space for deposits (Haapala and Lukkari, 2005; Pirajno, 2009).

In the Middle Jurassic, the Izanagi Plate started to subduct beneath the Euro-Asian Plate (perhaps multi-direction compressional and convergent tectonic system in eastern China, after Dong et al., 2008). The velocity of the subduction reached its apex at Late Jurassic (Wu et al., 2000) and the whole eastern China (including the Nanling Range) was under the maximal compression (Mercier et al., 2007; Wang et al., 2011a,b). Significant volume of granitic melt could be generated during the regional compression due to (1) the increasing geothermal gradient along with the crustal thickening (Brown, 1994; Yenes et al., 1999), (2) the friction heat from the movement of the thrust faults in the shear zone (Reavy, 1989), and (3) the accumulation of the metamorphic fluids (Newton, 1990). In the consequence, the syn-orogenic granitic magmas could be generated (Reavy, 1989; Newton, 1990; Brown, 1994; Pe-pier et al., 1998; Yenes et al., 1999). With increasing strength of the compression, the granitic magma in a deep-seated magma chamber could move upward along the crustal compressive-shearing faults (Petford and Atherton, 1992; Pe-pier et al., 1998) due to the "forceful mechanisms" (Castro and Fernandez, 1998). The magma could emplace in the form of syn-orogenic granite in the upper crust. The Yaogangxian biotite monzogranite shows following clear *syn*-orogenic features: (1) Its emplacement was controlled by the main deep-fault in this area (Huang, 2004); (2) The major emplacement took place at 155.4 Ma (Li et al., 2011a); (3) The rock shows crustal origin based on its mineralogy and geochemistry (Chen, 1988; Sun et al., 2009; Chen et al., 2011); (4) The rock formed from unfractionated granitic magmas based on presence of high-melting-point minerals (i.e., Ca-plagioclase, biotite, apatite, zircon) (Wang, 2008); (5) The biotite monzogranite has relatively high contents of basic major elements (Fe, Mg, Ca, Ti and P, Fig. 9a), the relatively high contents of compatible trace elements (Ba, Co, Cr, Hf, Ni, Sr, V, Zr), and the low contents of incompatible elements (Be, Cs, Li, Nb, Pb, Rb, Sn, Ta, Th, U, W, Y), comparing to the muscovite alkali-feldspar granite (Fig. 9a); and (6) The biotite monzogranite shows LREE-enriched REE patterns without pronounced negative Eu anomalies (Fig. 9b). These syn-orogenic characters indicate that the biotite-monzogranitic magma stayed for a relatively short period in the deep-seated magma chamber, the rock chemistry might represent the initial magma chemistry during the formation of the deep-seated magma chamber. Consequently, the crystallization age of the biotite monzogranite could represent the formation age of the deep-seated magma chamber. There might be a short temporal interval from the generation of magma to the emplacement and consolidation of the biotite-monzogranitic batholith.

The stress field in the Nanling Range (including the Yaogangxian area) converted from compressional to extensional at ~140 Ma (Gilder et al., 1996; Li, 1999; Ren et al., 1999). In the Early Cretaceous, the Nanling Range entered the extensional regime (Li et al., 1997, 2007; Hua et al., 2005), manifested by the presence of large amount of basic–intermediate veins (Li et al., 1997; Hua et al., 2005) and A-type granite intrusions (Li, 1999). Therefore, the timing of the emplacement of the Yaogangxian muscovite alkali-feldspar granite (133.4 Ma) and the formation of the tungsten ore (133.7 Ma) in the Yaogangxian area were perfectly fit in this extensional episode in the Nanling Range. In fact, the wolframite-bearing quartz veins in the Yaogangxian deposit are mainly distributing in NNW–NWW-trending extensional-shearing structures (Chen, 1981; Huang, 2004). The NW-trending diabase and

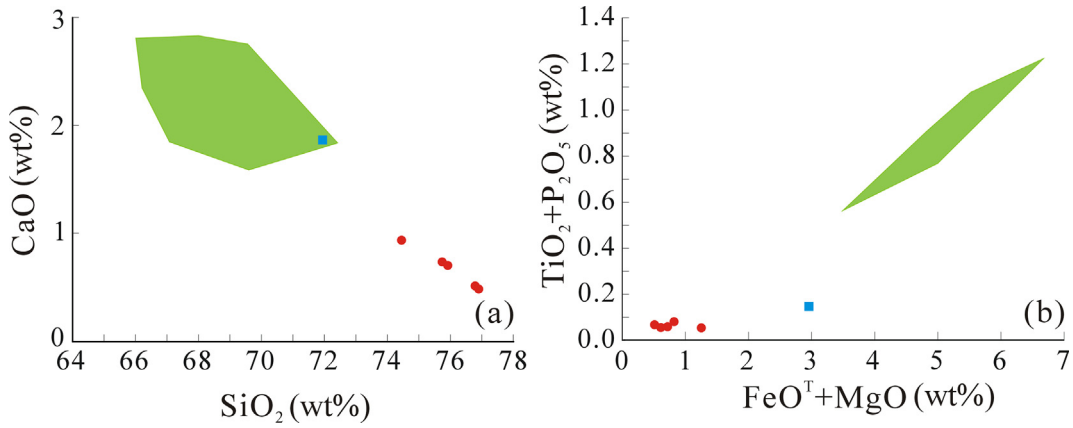

Fig. 8. Diagrams of whole-rock major elements for the biotite monzogranite and muscovite alkali-feldspar granite in the Yaogangxian pluton and its neighboring area (data from Table 3). (a) SiO_2 (wt%) versus CaO (wt%); (b) (FeO^T + MgO) (wt%) versus (TiO_2 + P_2O_5) (wt%). Blue solid square-Yaogangxian biotite monzogranite; Red solid dots-Yaogangxian muscovite alkali-feldspar granite; Green shadow area-Biotite monzogranite in the region. (For interpretation of the references to color in this figure legend, the reader is referred to the web version of this article.)

lamprophyre veins were also emerged at this period (Guo et al., 2010; He, 2002).

5.3. Ore-forming process

Based on above considerations, it is reasonable to conclude that the Yaogangxian tungsten deposit should form at 133.7 Ma, and its parental rock should be the muscovite alkali-feldspar granite. However, the Yaogangxian muscovite alkali-feldspar granite has two features which seem not favorable for the tungsten mineralization: (1) Its W content (4.8–11.0 ppm W, Table 4) is not very high (even if 50% of tungsten of this granite had moved into hydrothermal fluid); (2) Its volume is distinctly small (1.2 km^2 outcrop for the Yaogangxian granitic pluton, Fig. 1). The muscovite alkali-feldspar granite with these features seems not sufficient enough to generate this huge tungsten deposit with tens of thousands of tonnes of WO_3 (He, 2002) through the crystal-fractionation process. Thus, we here propose a new model to explain the possible ore-forming process of the Yaogangxian deposit.

The Yaogangxian deposit is characterized by the co-existing of biotite monzogranite, muscovite alkali-feldspar granite, and wolframite-bearing quartz veins. The biotite monzogranite formed at 155 Ma under a compressive regime while the muscovite alkali-feldspar granite and the wolframite-bearing quartz veins formed at 133 Ma under an extensional regime. The observations listed below will help us to decipher the relationships among the biotite monzogranite, the muscovite alkali-feldspar granite, and the wolframite-bearing quartz veins.

(1) In the Yaogangxian deposit, the wolframite-bearing quartz veins crosscut and extend more than one thousand meters downwards into the biotite monzogranite (Fig. 2a) (Chen, 1981). For some veins, a progressive transition can be observed downwards from the wolframite-bearing quartz vein via pegmatitic or aplitic vein to the fine-grained muscovite alkali-feldspar granite vein (Chen, 1988). Based on these spatial relationships, it is reasonable to assume that a hidden muscovite alkali-feldspar granite stock, occurring beneath the biotite monzogranite (Guo et al., 2010), should be the real parental rock of the Yaogangxian deposit.
(2) Due to incomplete segregating, the melt could contain a small quantity of alkaline and siliceous fluid rich in the incompatible components (i.e., halogens, ore metals) and hydrothermal zircon can precipitate with ore minerals and volatile-rich minerals in the fluid-rich muscovite alkali-feldspar granite. By the way, the fact that the muscovite alkali-feldspar granite does not contain ~133 Ma magmatic zircon indicates that the highly-fractionated magma raised relatively rapidly and might have dumped most of the high-melting-point minerals (i.e., Fe–Ti oxides, zircon, apatite, biotite, Ca-plagioclase) through fractional crystallization in the deep-seated magma chamber.
(3) The relict zircon, occurring as cores included within the hydrothermal zircon within the muscovite alkali-feldspar granite and the wolframite-bearing quartz veins, is extremely similar to the magmatic zircon from the biotite monzogranite in morphology, chemistry and crystallization age. These relict zircon cores could be captured during the ascent of the residual melt, indicating that the wolframite-bearing quartz veins and the muscovite alkali-feldspar granite should have used the same passages (i.e., faults) during their emplacement into the upper crust.
(4) Because of the ultra-long duration of crystal fractionation in the deep-seated magma chamber, the residual melt at the top of the magma chamber should be extremely enriched in the incompatible ore-forming materials (alkali, halogens, tungsten, and aqueous fluid). Therefore, the huge amount of tungsten for the Yaogangxian deposit could be derived from the relatively small muscovite alkali-feldspar granite stocks. Many mineral deposits hosted in alkaline magmatic rocks have also been inferred to be related to the magmatic fractionation in deep-seated magma chambers (Halter and Webster, 2004; Muller et al., 2009).

Based on the integration of all data and observations, a new mineralization model is proposed as follows:

(1) The syn-orogenic biotite monzogranite emplaced at 155 Ma with origins from a deep-seated magma chamber, which continued its evolution through fractional crystallization during the whole orogenic event. The thermal and gravitational convection retained its

Table 4
Trace-element concentrations (in ppm) of biotite monzogranites and muscovite alkali-feldspar granites in the Yaogangxian pluton and its neighboring area.

Rock	Biotite monzogranite															Muscovite alkali-feldspar granite				
Sample	c–10a	c–10b	c–10d	c–10e	c–12	c–15	c–16	c–17	c–18	c–22a	c–26	c–27a	c–27b	c–27c	19–3	YGX–34	YGX–36	YGX–37	YGX–2	YGX–3
Ba	818.9	1078.1	652.2	447.7	509.9	469.1	711.3	416.3	905.4	518.0	262.7	1042.9	737.9	489.3	458.0	8.5	6.3	31.0	16.3	23.1
Be	ND	ND	ND	ND	ND	ND	ND	ND	ND	ND	ND	ND	ND	ND	ND	13.0	8.5	3.8	11.9	6.3
Co	4.3	6.3	5.0	7.3	7.0	6.0	6.4	6.6	5.6	4.8	4.2	7.5	40.5	9.0	3.0	ND	ND	ND	0.4	0.3
Cr	10.0	11.0	9.3	12.5	10.6	10.0	27.7	10.4	13.9	31.1	17.4	13.4	14.9	13.3	5.9	ND	ND	ND	1.1	1.3
Cs	16.6	13.8	16.6	17.5	51.2	43.7	24.8	16.0	15.2	23.7	30.9	12.4	12.3	12.2	ND	35.0	28.0	38.0	20.2	52.3
Hf	ND	ND	ND	ND	ND	ND	ND	ND	ND	ND	ND	ND	ND	ND	4.7	4.8	6.2	4.0	5.5	4.5
Li	ND	ND	ND	ND	ND	ND	ND	ND	ND	ND	ND	ND	ND	ND	67.3	112.0	173.0	282.0	59.3	309.0
Nb	23.0	23.4	19.3	30.6	26.9	21.1	22.9	23.9	15.7	21.0	25.3	23.1	30.3	29.4	17.3	39.0	15.0	41.0	46.4	34.9
Ni	4.4	4.6	3.7	5.2	4.9	7.0	12.3	4.7	4.9	15.7	9.8	4.8	7.3	5.8	2.6	ND	ND	ND	0.8	0.7
Pb	ND	ND	ND	ND	ND	ND	ND	ND	ND	ND	ND	ND	ND	ND	47.6	61.0	44.0	50.0	80.3	79.5
Rb	422.2	387.2	420.6	293.3	433.4	468.3	312.5	260.3	262.3	383.9	400.0	274.8	260.3	238.5	793.0	719.0	765.0	917.0	604.8	252.8
Sn	ND	ND	ND	ND	ND	ND	ND	ND	ND	ND	ND	ND	ND	ND	51.2	25.0	42.0	36.0	8.1	20.8
Sr	223.3	230.3	177.0	176.4	183.3	159.2	176.3	162.4	320.8	144.6	111.5	227.6	214.0	222.6	18.3	4.7	3.2	8.0	7.4	11.1
Ta	ND	ND	ND	ND	ND	ND	ND	ND	ND	ND	ND	ND	ND	ND	2.3	13.0	8.0	11.0	27.6	11.5
Th	ND	ND	ND	ND	ND	ND	ND	ND	ND	ND	ND	ND	ND	ND	18.5	19.0	16.0	21.0	13.7	23.4
U	ND	ND	ND	ND	ND	ND	ND	ND	ND	ND	ND	ND	ND	ND	17.3	21.0	15.0	20.0	31.4	31.1
V	33.5	37.4	26.0	44.6	40.5	32.2	34.8	36.1	31.4	25.2	20.5	39.8	56.0	54.7	6.1	0.7	0.6	1.6	1.6	1.2
W	ND	ND	ND	ND	ND	ND	ND	ND	ND	ND	ND	ND	ND	ND	ND	4.8	7.1	11.0	6.6	7.5
Y	41.4	42.0	31.6	47.2	44.6	38.7	37.1	38.5	42.2	34.2	40.1	41.4	48.3	44.5	ND	145.0	164.0	83.0	80.5	38.7
Zr	233.5	289.2	208.2	307.1	237.7	227.9	181.8	203.9	266.1	173.2	164.4	215.5	316.4	299.1	148.0	71.0	65.0	75.0	59.0	65.4

Note: ND—Not Determined. Data source: Samples c–10a, c–10b, c–10d, c–10e, c–12, c–15, c–16, c–17, c–18, c–22a, c–26, c–27a, c–27b, c–27c from the Qitianling pluton (Deng et al., 2005); Sample 19–3 from the Yaogangxian pluton (Wang, 2008); Samples YGX–34, YGX–36 and YGX–37 from the Yaogangxian pluton (Xie et al., 2013); Samples YGX–2 and YGX–3 from the Yaogangxian pluton (this study).

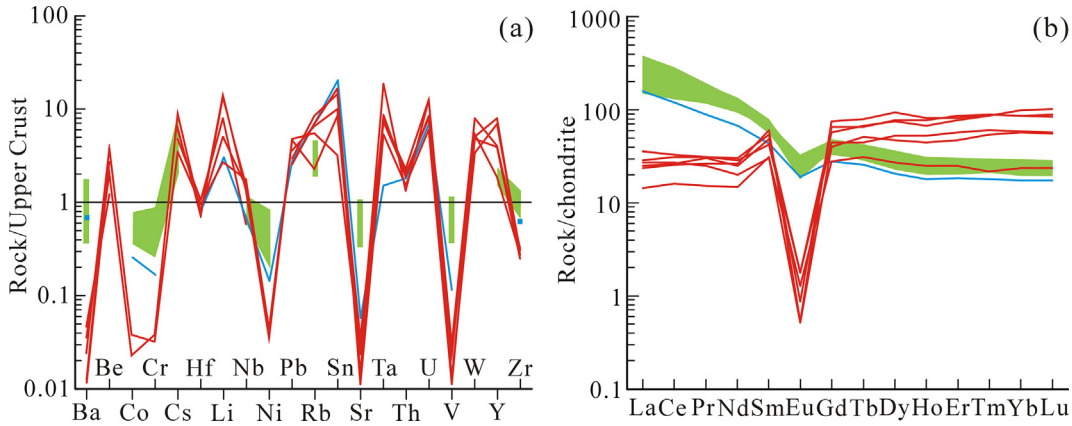

Fig. 9. Comparison of trace element data between the biotite monzogranite and the muscovite alkali-feldspar granite in the Yaogangxian pluton and its neighboring area. (a) Multi-element spider diagrams normalized to Upper Crust composition (Wedepohl, 1995) (data from Table 4); (b) REE diagram normalized to Chondrite values (Taylor and McLennan, 1985) (data from Table 5). Blue line-Yaogangxian biotite monzogranite; Red lines-Yaogangxian muscovite alkali-feldspar granite; Green shadow area-Biotite monzogranite in the region. (For interpretation of the references to color in this figure legend, the reader is referred to the web version of this article.)

activity in the magma chamber (Sparks, 1990), allowing the high-melting-point minerals (i.e., the volatile-free accessory minerals, ferromagnesian minerals, Ca-plagioclase) to crystallize and sink to the bottom of the magma chamber. Conversely, the incompatible elements, which includes alkali (Na, K, Li) (Veksler, 2004), halogens (F, Cl, B) (Villemant and Boudon, 1999; Boissard et al., 2010), metal elements (W, Sn, Nb, Ta, REE) (Christiansen et al., 1986; Raimbault et al., 1987) and aqueous fluid (Boissard et al., 2010), remained in the melt and concentrated upwards toward the top of the deep-seated magma chamber (Frial and Spera, 1990; Haapala and Lukkari, 2005).

(2) At ~140 Ma, the tectonic regime in the southeast China (including the Nanling Range) converted from shearing-compression to shearing-extension (Gilder et al., 1996; Li, 1999; Ren et al., 1999) due to the change of subduction direction of the Izanagi plate (Engebretson et al., 1985; Maruyama et al., 1997). The previous shearing-compressive faults formed during the Late Jurassic revived and changed into shearing-extensional faults after 140 Ma (Gilder et al., 1996; Li and Mei, 1999; Jia and Hu, 2002). Highly-fractionated granitic melt was extracted from deep-seated magma chamber (Bachmann and Bergantz, 2008) and ascend rapidly due to the "permissive mechanisms" (Castro and Fernandez, 1998), forming the post-orogenic granitic intrusion (i.e., the muscovite alkali-feldspar granite). In general, the life spans of the deep-seated magma chamber are from 1.4 Myr to a maximum of ~10 Myr (Coleman et al., 2004). However, based on a geothermal model proposed by Gudmundsson (2012), magma chamber with a volume of ~1000 km^3 (Lipman, 1984; Degruyter and Huber, 2014) in the middle crust can maintain partially molten for over 20 Myr and many cases of long-lived melt have been reported. For instance, the well-known Variscan orogenic belt (Europe), formed during the continental collision between Gondwana and Laurasia, has its batholithic biotite monzogranites dated between 342 and 331 Ma, the satellitic muscovite alkali-feldspar granites dated between 319 and 308 Ma (Alexandre et al., 2002), and a mean age difference between the biotite monzogranite and the muscovite alkali-feldspar granite is ~23 Myr. A similar case can be found in the Quérigut pluton (Pyrénées, France) where the 270–280 Ma satellitic leucogranite is surrounded by the ~20 Myr older batholithic monzogranite (Auréjac et al., 2004). Thus, a deep-seated magma chamber, generated by crustal thickening in the middle crust, can survive more than 20 Myr.

(3) During the emplacement of the residual magma in the extensional setting, the solubility of fluids would reduce quickly due to the sudden decompression and sharp reduction of magma temperature. Accordingly, the residual magma could separate into two portions (i.e., fluid–melt immiscibility): the melt-bearing alkaline–siliceous fluid and the fluid-bearing alkaline–felsic melt (Veksler, 2004; Suk, 2012). The melt-bearing alkaline–siliceous fluid has higher mobility due to its lower density and less viscosity, allowing it to move ahead of the granitic melt and form the ore on top of the granite body. Since tungsten has high solubility in the F-enriched alkaline–siliceous fluid (Webster and De Vivo, 2002; Veksler, 2004), it was concentrated in the fluid portion during fluid–melt separation when the immiscibility increased along with the dropping of P–T in the igneous system, forming the wolframite-bearing quartz veins in the extensional system. The fluid-bearing alkaline–felsic melt moved behind the fluid portion and solidified in the lower part of the extensional system to form the muscovite alkali-feldspar granite.

6. Conclusions

Morphology, geochemistry and geochronology of zircon from the muscovite alkali-feldspar granite and the wolframite-bearing quartz veins in the Yaogangxian deposit reveal that the zircon crystals have two genetic types, the hydrothermal zircon and the magmatic zircon.

Based on systematic analysis of the geochronological and isotopic features of the zircon crystals, the field relationship between ore, muscovite alkali-feldspar granite and biotite monzogranite, as well as the regional tectonic evolution, we propose the ore-forming process of the Yaogangxian tungsten deposit as follows: (1) A deep-seated magma chamber formed under syn-orogenic regime at ca. 155 Ma; (2) A highly-differentiated magma gathered from the ultra-long fractionated deep-

Table 5
Rare earth element data (in ppm) of biotite monzogranites and muscovite alkali-feldspar granites in the Yaogangxian pluton and its neighboring area.

Rock	Biotite monzogranite															Muscovite alkali-feldspar granite					
编号	c–10a	c–10b	c–10d	c–10e	c–12	c–15	c–16	c–17	c–18	c–22a	c–26	c–27a	c–27b	c–27c	19–3	C70	YGX–34	YGX–36	YGX–37	YGX–2	YGX–3
La	77.03	57.65	84.23	74.21	80.66	64.18	89.77	84.14	53.86	70.47	79.04	35.43	52.95	40.79	37.40	5.92	6.8	5.7	8.4	3.47	6.42
Ce	143.98	114.99	149.44	147.95	153.55	122.72	178.85	151.05	108.92	128.69	141.73	79.42	112.04	92.93	73.50	16.22	19	16	20	10.00	16.94
Pr	16.2	14.01	15.95	17.62	17.55	14.16	18.08	16.52	13.77	14.21	15.64	10.76	14.61	12.47	8.32	2.84	2.9	2.5	2.9	1.42	2.32
Nd	54.91	50.46	51.18	62.07	59.91	49.18	60.02	54.57	52.45	47	50.67	43.31	55.89	48.69	30.50	11.57	14	12	13	6.84	9.31
Sm	9.87	9.83	8.3	11.64	10.88	9.3	10.12	9.5	10.61	8.16	8.94	9.39	11.38	10.15	6.46	7.29	8	9	6.2	4.69	4.56
Eu	1.58	1.68	1.3	1.49	1.49	1.37	1.47	1.36	1.87	1.23	1.01	1.72	1.65	1.51	1.08	0.10	0.05	0.03	0.1	0.03	0.07
Gd	8.47	8.51	6.7	9.55	9.11	7.85	8.08	7.76	9.51	6.67	7.39	8.6	9.76	8.76	5.53	11.46	13	15	9	7.89	5.60
Tb	1.33	1.34	1.04	1.51	1.42	1.24	1.22	1.22	1.42	1.07	1.2	1.34	1.55	1.38	0.92	2.47	2.4	2.9	1.6	1.84	1.13
Dy	7.59	7.57	5.73	8.48	7.89	6.97	6.7	6.86	7.89	5.99	6.84	7.57	8.85	7.91	5.05	18.54	19	23	13	11.68	6.67
Ho	1.49	1.48	1.11	1.66	1.56	1.36	1.31	1.34	1.5	1.16	1.36	1.46	1.72	1.55	0.99	3.68	4.2	4.5	2.9	2.47	1.36
Er	4.27	4.29	3.25	4.83	4.55	3.91	3.73	3.92	4.12	3.45	3.99	4.09	4.92	4.45	2.94	12.44	14	13	9.2	7.62	4.04
Tm	0.66	0.67	0.52	0.75	0.7	0.62	0.57	0.61	0.61	0.56	0.64	0.63	0.74	0.67	0.44	2.11	2.2	2.2	1.5	1.33	0.54
Yb	4.19	4.19	3.18	4.72	4.47	3.8	3.52	3.76	3.62	3.51	4.04	3.79	4.54	4.19	2.84	16.13	14	14	9.5	9.31	3.87
Lu	0.62	0.63	0.48	0.7	0.67	0.57	0.52	0.56	0.53	0.52	0.6	0.56	0.67	0.62	0.43	2.50	2.2	2.1	1.4	1.37	0.58
LREE	303.6	248.6	310.4	315.0	324.0	260.9	358.3	317.1	241.5	269.8	297.0	180.0	248.5	206.5	157.3	43.9	50.8	45.2	50.6	26.5	39.6
HREE	28.6	28.7	22.0	32.2	30.4	26.3	25.7	26.0	29.2	22.9	26.1	28.0	32.8	29.5	19.1	69.3	71.0	76.7	48.1	43.5	23.8
Eu/Eu*	0.53	0.56	0.53	0.43	0.46	0.49	0.50	0.48	0.57	0.51	0.38	0.58	0.48	0.49	0.55	0.03	0.01	0.01	0.04	0.01	0.04

Note: $Eu/Eu^* = Eu_n/(Sm_n \times Gd_n)^{0.5}$. Data source: Samples c–10a, c–10b, c–10d, c–10e, c–12, c–15, c–16, c–17, c–18, c–22a, c–26, c–27a, c–27b, c–27c from the Qitianling pluton (Deng et al., 2005); Sample 19–3 from the Yaogangxian pluton (Wang, 2008); Sample C70 from the Yaogangxian pluton (Wu et al., 2008); Samples YGX–34, YGX–36 and YGX–37 from the Yaogangxian pluton (Xie et al., 2013); Samples YGX–2 and YGX–3 from the Yaogangxian pluton (this study).

Table 6
Hydrothermal zircon Hf isotopes from the wolframite-bearing quartz vein (YGX–6) and the muscovite alkali-feldspar granite (YGX–2) in the Yaogangxian tungsten deposit.

Sample	Spot	t (Ga)	$^{176}Lu/^{177}Hf$	$^{176}Hf/^{177}Hf$	Hf_i	± 2	T_{DM} (Ga)	$_{Hf}(t)$
YGX–6	#1	0.1341	0.001901	0.282128	0.282123	0.000060	1.57	−19.9
	#2	0.1341	0.001662	0.282175	0.282171	0.000074	1.49	−18.2
	#3	0.1341	0.005114	0.282360	0.282347	0.000093	1.37	−12.0
	#4	0.1341	0.001358	0.282331	0.282328	0.000093	1.27	−12.7
YGX–2	#1	0.1335	0.002413	0.282134	0.282128	0.000056	1.58	−19.7
	#2	0.1335	0.000674	0.282186	0.282185	0.000089	1.44	−17.8
	#3	0.1335	0.001422	0.282407	0.282404	0.000147	1.17	−10.0
	#4	0.1335	0.002186	0.282212	0.282206	0.000153	1.46	−17.0

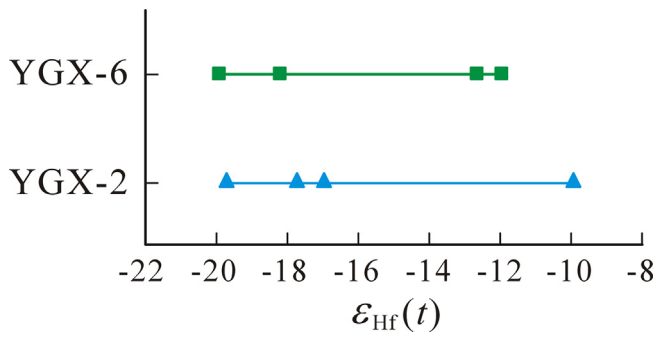

Fig. 10. Comparison of hydrothermal zircon $\varepsilon_{Hf}(t)$ values between the muscovite alkali-feldspar granite (blue solid triangles-YGX–2) and the wolframite-bearing quartz veins (green solid squares-YGX–6) in the Yaogangxian tungsten deposit (data from Table 6). (For interpretation of the references to color in this figure legend, the reader is referred to the web version of this article.)

seated magma chamber; (3) Muscovite alkali-feldspar granite and wolframite-bearing quartz veins formed by the fluid–melt immiscibility of the highly-fractionated residual magma during the post-orogenic regime at ca. 133 Ma.

Acknowledgements

Dr. Shunting Li is acknowledged for providing one excellent photo on intrusive contact between the biotite monzogranite and the muscovite alkali-feldspar granite (Fig. 2b). We thank two anonymous reviewers for their insightful comments for the first submission of this manuscript and we also thank those who read and help to make corrections for different versions of this manuscript. The guest editor Dr. Zhou, M.F. is thanked heartily for spending tremendous time helping improve the paper. This study is supported by the National Natural Science Foundation of China (Project No. 41372065).

References

Alexandre, P., Carlier, Le, de Veslud, C., Cuney, M., Ruffet, G., Virlogeux, D., Cheilletz, A., 2002. Datation $^{40}Ar/^{39}Ar$ des leucogranites sous couverture du complexe plutonique de Charroux-Civray (Vienne). Comptes Rendus Geoscience 334, 1141–1148.
Audétat, A., Gunther, D., Heinrich, C.A., 2000. Magmatic-hydrothermal evolution in a fractionating granite: a microchemical study of the Sn–W–F-mineralized Mole Granite (Australia). Geochimica et Cosmochimica Acta 64, 3373–3393.
Auréjac, J.B., Gleizes, G., Diot, H., Bouchez, J.L., 2004. The Quérigut Complex (Pyrénées, France) revisited by the AMS technique: a syntectonic pluton of the Variscan dextral transpression. Bulletin de la Societé Géologique de France 175, 157–174.
Bachmann, O., Bergantz, G.W., 2008. Rhyolites and their source mushes across tectonic settings. J. Petrol. 49, 2277–2285.
Badanina, E.V., Veksler, I.V., Thomas, R., Syritso, L.F., Trumbull, R.B., 2004. Magmatic evolution of Li–F, rare-metal granites: a case study of melt inclusions in the Khangilay complex, Eastern Transbaikalia (Russia). Chem. Geol. 210, 113–133.
Barton, M.D., 1987. Lithophile-element mineralization associated with Late Cretaceous two-mica granites in the Great Basin. Geology 15, 337–340.
Bastos Neto, A.C., Pereira, V.P., Ronchi, L.H., de Lima, E.F., Frantz, J.C., 2009. The world-class Sn, Nb, Ta, F (Y, REE, Li) deposit and the massive cryolite associated with the albite-enriched facies of the Madeira A-type granite, Pitinga mining district, Amazonas state, Brazil. Canadian Mineralogist 47, 1329–1357.
Boissard, H.B., Villemant, B., Boudon, G., 2010. Behavior of halogens during the degassing of felsic magmas. Geochem. Geophys. Geosyst. 11, 1–22.
Brown, M., 1994. The generation, segregation, ascent and emplacement of granite magma: the migmatite-to-crustally-derived granite connection in thickened orogens. Earth Sci. Rev. 36, 83–130.
Castro, A., Fernandez, C., 1998. Granite intrusion by externally induced growth and deformation of magma reservoir, the example of the Plasenzuela pluton, Spain. J. Struct. Geol. 20, 1219–1228.
Černý, P., Masau, M., Goad, B.E., Ferreira, K., 2005. The Greer Lake leucogranite, Manitoba, and the origin of lepidolite-subtype granitic pegmatites. Lithos 80, 305–321.
Chen, H.W., Hu, R.Z., Peng, J.T., Bi, X.W., 2011. Helium and argon isotopic compositions of ore-forming fluid from the Yaogangxian tungsten deposit and their geological implications. Acta Mineralogica Sinica 31, 597–603 (in Chinese with English abstract).
Chen, Y.R., 1981. Geological features and ore-prospecting indications in the Yaogangxian vein-type tungsten deposit. Geol. Prospect. 17, 25–30 (in Chinese with English abstract).
Chen, Y.R., 1988. Geological and geochemical characteristics and diagenetic-minerogenetic processes of Yaogangxian granite. Mineral Resour. Geol. 2, 62–72 (in Chinese with English abstract).
Christiansen, E.H., Sheridan, M.F., Burt, D.M., 1986. The geology and geochemistry of Cenozoic topaz rhyolites from the western United States. Geol. Soc. Am. Spec. Pap. 205, 1–82.
Claoué-Long, J.C., King, R.W., Kerrich, R., 1990. Archaean hydrothermal zircon in the Abitibi greenstone belt: constraints on the timing of gold mineralization. Earth Planet. Sci. Lett. 98, 109–128.
Coleman, D.S., Gray, W., Glazner, A.F., 2004. Rethinking the emplacement and evolution of zoned plutons: Geochronologic evidence for incremental assembly of the Tuolumne Intrusive Suite, California. Geology 32, 433–436.
Degruyter, W., Huber, C., 2014. A model for eruption frequency of upper crustal silicic magma chambers. Earth Planet. Sci. Lett. 403, 117–130.
Deng, X.G., Li, X.H., Liu, Y.M., Huang, G.F., Hou, M.S., 2005. Geochemical characteristics of Qitianling granites and their implications for mineralization. Acta Petrologica et Mineralogica 24, 93–102 (in Chinese with English abstract).
Dong, S.W., Zhang, Y.Q., Chen, X.H., Long, C.X., Wang, T., Yang, Z.Y., Hu, J.M., 2008. The Formation and Deformational Characteristics of East Asia Multi-Direction Convergent Tectonic System in Late Jurassic. Acta Geoscientica Sinica 29, 306–317 (in Chinese with English abstract).
Engebretson, D.C., Cox, A., Gordon, R.G., 1985. Relative motions between oceanic and continental plates in the Pacific basin. Geol. Soc. Am. Spec. Pap. 206, 1–59.
Farrar, E., Yamamura, B.K., Clark, A.H., Taipe, J.A., 1990. $^{40}Ar/^{39}Ar$ ages of magmatism and tungsten–polymetallic mineralization, Palca 11, Choquene District, southeastern Peru. Econ. Geol. 85, 1669–1676.
Forster, H.J., Tischendorf, G., Trumbull, R.B., Gottesmann, B., 1999. Late-collisional granites in the Variscan Erzgebirge, Germany. J. Petrol. 40, 1613–1645.
Frial, A.F., Spera, F.J., 1990. Mechanisms for the generation of compositional heterogeneities in magma chambers. Geol. Soc. Am. Bull. 102, 353–367.
Gilder, S.A., Gill, J., Coe, R.S., Zhao, X.X., Liu, Z.W., Wang, G.X., Yuan, K.R., Liu, W.L., Kuang, G.D., Wu, H.R., 1996. Isotopic and paleomagnetic constrains on the Mesozoic tectonic evolution of South China. J. Geophys. Res. Solid Earth Sect. 101, 16137–16154.
Groves, D.I., Bierlein, F.P., 2007. Geodynamic settings of mineral deposit systems. J. Geol. Soc. 164, 19–30.
Gudmundsson, A., 2012. Magma chambers: Formation, local stresses, excess pressures, and compartments. J. Volcanol. Geoth. Res. 237–238, 19–41.
Guo, W.G., Jiang, J.Z., Gan, X.P., 2010. Research on the ore deposit geologic characteristics and metallogenic model of Yaogangxian tungsten deposit, Hunan Province. Mineral Resour. Geol. 24, 308–313 (in Chinese with English abstract).
Haapala, I., Lukkari, S., 2005. Petrological and geochemical evolution of the Kymi stock, a topaz granite cupola within the Wiborg rapakivi batholith, Finland. Lithos 80, 347–362.
Halter, W.E., Webster, J.D., 2004. The magmatic to hydrothermal transition and its bearing on ore-forming systems. Chem. Geol. 210, 1–6.

He, X.P., 2002. A prediction on looking for mineral deposit in Yaogangxian tungsten mine. China Tungsten Ind. 17, 39–43 (in Chinese with English abstract).
Heinhorst, J., Lehmann, B., 1995. Rare-metal granite magmatism and crustal evolution of Central Kazakhstan: A reconnaissance study. In: Pasava, J., Kribek, B., Zak, K. (Eds.), Mineral Deposits: from their origin to their environmental impacts. Balkema, Rotterdam, pp. 455–458.
Higgins, N.C., 1985. Wolframite deposition in a hydrothermal vein system: the Grey River tungsten prospect, Newfoundland, Canada. Econ. Geol. 80, 1297–1327.
Hoskin, P.W.O., 2005. Trace-element composition of hydrothermal zircon and the alteration of Hadean zircon from the Jack Hills, Australia. Geochimica et Cosmochimica Acta 69, 637–648.
Hua, R.M., Chen, P.R., Zhang, W.L., Yao, J.M., Lin, J.F., Zhang, Z.S., Gu, S.Y., 2005. Metallogenesis and their geodynamic settings related to Mesozoic granitoids in the Nanling Range. Geol. J. China Univ. 11, 291–304 (in Chinese with English abstract).
Huang, C.J., 2004. Wolframite rank alternate derive develop theory of Yaogangxian mine in Hunan. Hunan Nonferrous Metals 20, 1–4 (in Chinese with English abstract).
Jia, D.C., Hu, R.Z., 2002. Tectonic setting discrimination of late Yanshanian granites in northeast Hunan Province. Geol. Geochem. 30, 10–14 (in Chinese with English abstract).
Kerrich, R., King, R., 1993. Hydrothermal zircon and baddeleyite in Val d'Or Archean mesothermal gold deposits; characteristics, compositions, and fluid–inclusion properties, with implications for timing of primary gold mineralization. Can. J. Earth Sci. 30, 2334–2351.
Lerouge, C., Deschamps, Y., Piantone, P., Gilles, C., Breton, J., 2007. Metal-carrier accessory minerals associated with W ± Sn mineralization, La Châtaigneraie tungsten ore district, Massif Central, France. Canadian Mineralogist 45, 875–889.
Li, H.Q., Lu, Y.F., Wang, D.H., Chen, Y.C., Yang, H.M., Guo, J., Xie, C.F., Mei, Y.P., Ma, L.Y., 2006. Dating of the rock-forming and ore-forming ages and their geological significances in the Furong orefield, Qitian Mountain, Hunan. Geol. Rev. 52, 113–121 (in Chinese with English abstract).
Li, S.T., Wang, J.B., Zhu, X.Y., Wang, Y.L., Han, Y., Guo, N.N., 2011a. Chronological characteristics of the Yaogangxian composite pluton in Hunan Province. Geol. Prospect. 47, 143–150 (in Chinese with English abstract).
Li, S.T., Wang, J.B., Zhu, X.Y., Li, C., 2011b. Re–Os dating of molybdenite and sulfur isotope analysis of the Yaogangxian tungsten polymetallic deposits in Hunan Province and their geological significance. Geoscience 25, 228–235 (in Chinese with English abstract).
Li, S.T., Zhu, X.Y., Wang, J.B., Wang, Y.L., Cheng, X.Y., Jiang, B.B., 2015. Geological and geochemical characteristics of the Yaogangxian complex granitoid and its relationship with tungsten mineralization. Mineral Exploration 6, 347–355 (in Chinese with English abstract).
Li, X.H., Hu, R.Z., Rao, B., 1997. Geochronology and geochemistry of Cretaceous mafic dikes from northern Guangdong, SE China. Geochimica 26, 14–31 (in Chinese with English abstract).
Li, X.H., 1999. Cretaceous magmatism and lithosphere extension in South China: The geochronology and geochemistry constraints. Resource Environment and Sustaining Development, Institute of Geochemistry, Chinese Academy of Sciences, Beijing, Science Press 264–273 (in Chinese).
Li, X.H., Li, W.X., Li, Z.X., 2007. On the genetic classification and tectonic implications of the Early Yanshanian granitoids in the Nanling Range, South China. Chin. Sci. Bull. 52, 1873–1885.
Li, Z.L., Mei, Y.W., 1999. The distribution regularity of tungsten deposits and the prognosis of concealed deposits in South Jiangxi. Jiangxi Geol. 13, 276–282 (in Chinese with English abstract).
Lipman, P.W., 1984. The roots of ash flow calderas in western North America; windows into the tops of granitic batholiths. J. Geophys. Res. 89, 8801–8841.
Liu, D.Y., 1994. Typomorphic peculiarities of quartz in the Yaogangxian tungsten deposit, Hunan. Acta Mineralogica Sinica 14, 74–82 (in Chinese with English abstract).
Mangas, I., Perez-Torrado, F.J., 1995. Fluid inclusion and stable isotope studies in Sn–W deposits of western Spain. In: Pasava, J., Kribek, B., Zak, K. (Eds.), Mineral Deposits: from their origin to their environmental impacts. Balkema, Rotterdam, pp. 473–476.
Mao, J.W., Li, H.Y., Song, X.X., 1998. Geology and Geochemistry of the Shizhuyuan W-Sn–Mo–Bi polymetallic deposit, Hunan, China. Geological Publishing House, Beijing 1–215 (in Chinese).
Mao, J.W., Li, X.F., Lehmann, B., Chen, W., Lan, X.M., Wei, S.L., 2004. ^{40}Ar–^{39}Ar dating of tin ores and related granite in Furong tin orefield, Hunan Province, and its geodynamic significance. Mineral Dep. 23, 164–175 (in Chinese with English abstract).
Maruyama, S., Isozaki, Y., Kimura, G., Terabayashi, M.C., 1997. Paleogeographic maps of the Japanese Islands: plate tectonic synthesis from 750 Ma to the present. Island Arc 6, 121–142.
Mercier, J.L., Hou, M.J., Vergély, P., Wang, Y.M., 2007. Structural and stratigraphical constraints on the kinematics history of the southern Tan–Lu Fault Zone during the Mesozoic Anhui province, China. Tectonophysics 439, 33–66.
Muller, A., van den Kerkhof, A.M., Behr, H.J., Kronz, A., Koh-Muller, M., 2009. The evolution of late-Hercynian granites and rhyolites documented by quartz: a review. Trans R. Soc. Edinb. Earth Environ. Sci. 100, 35–49.
Newton, R.C., 1990. Fluids and shear zones in the deep crust. Tectonophysics 182, 21–37.
Pan, L., Cai, X.H., 2009. Ore-forming elements and prospecting direction. Land Resour. Herald 2, 54–59 (in Chinese).
Pe-pier, G., Koubouvelas, I., Davis, J.W., 1998. Synkinematic granite emplacement in a shear zone: the Pleasant Hills pluton, Canadian Appalachians. Geol. Soc. Am. Bull. 110, 523–536.
Pelleter, E., Cheilletz, A., Gasquet, D., Mouttaqi, A., Annich, M., El Hakour, A., Deloule, E., Féraud, G., 2007. Hydrothermal zircons: A tool for ion microprobe U-Pb dating of gold mineralization (Tamlalt–Menhouhou gold deposit, Morocco). Chem. Geol. 245, 135–161.
Peng, J.T., Zhou, M.F., Hu, R.Z., Shen, N.P., Yuan, S.D., Bi, X.W., Du, A.D., Qu, W.J., 2006. Precise molybdenite Re–Os and mica Ar–Ar dating of the Mesozoic Yaogangxian tungsten deposit, central Nanling district, South China. Mineralium Deposita 41, 661–669.
Petford, N., Atherton, M.P., 1992. Granitoid emplacement and deformation along a major crustal lineament: the Cordillera Blanca, Peru. Tectonophysics 205, 171–185.
Pirajno, F., 2009. Hydrothermal processes and mineral systems. Springer 1–1250.
Pupin, J.P., 1980. Zircon and granite petrology. Contrib. Miner. Petrol. 73, 207–220.
Raimbault, L., Meyer, G., Treuil, M., 1987. Comportements differenciés de W, Sn, U, Ta, Nb dans quelques complexes granitiques du Massif Central français. Bulletin de Minéralogie 110, 591–601.
Reavy, R.J., 1989. Structural controls on metamorphism and syn-tectonic magmatism: the Portuguese Hercynian collision belt. J. Geol. Soc. (Lond.) 146, 649–657.
Ren, J.S., Wang, Z.X., Chen, B.W., Jiang, C.F., Niu, B.G., Li, J.R., Xie, G.L., He, Z.J., Liu, Z.G., 1999. The tectonics of China from a global view: a guide to the tectonic map of China and adjacent regions. Geological Publishing House, Beijing 1–25 (in Chinese).
Rubin, J.N., Henry, C.D., Price, J.G., 1989. Hydrothermal zircon at zircon overgrowths, Sierra Blanca Peaks, Texas. Am. Mineral. 74, 865–869.
Rubin, J.N., Henry, C.D., Price, J.G., 1993. The mobility of zirconium and other "immobile" elements during hydrothermal alteration. Chem. Geol. 110, 29–47.
Sparks, R.S.J., 1990. Crystal capture, sorting, and retention in convecting magma: Discussion. Geol. Soc. Am. Bull. 102, 847–848.
Suk, N.I., 2012. Experimental study of liquid immiscibility in the fluid–magmatic silicate systems containing Ti, Nb, Sr, REE, and Zr. Petrology 20, 138–146.
Sun, J., Ni, Y.J., Bai, D.Y., Ma, T.Q., 2009. Geochemistry, petrogenesis and tectonic setting of early Yanshanian Yaogangxian granite pluton, southeastern Hunan province. Geol. Mineral Resour. South China 25, 12–18 (in Chinese with English abstract).
Suwimonprecha, P., Černý, P., Friedrich, G., 1995. Rare metal mineralization related to granites and pegmatites, Phuket, Thailand. Econ. Geol. 90, 603–615.
Taylor, S.R., McLennan, S.M., 1985. The continental crust: Its composition and evolution. Blackwell, Oxford Press, pp. 1–312.
Thomas, R., Forster, H.J., Rickers, K., Webster, J.D., 2005. Formation of extremely F-rich hydrous melt fractions and hydrothermal fluids during differentiation of highly evolved tin-granite magmas: A melt/fluid-inclusion study. Contrib. Miner. Petrol. 148, 582–601.
Veksler, I.V., 2004. Liquid immiscibility and its role at the magmatic-hydrothermal transition: a summary of experimental studies. Chem. Geol. 210, 7–31.
Villemant, B., Boudon, G., 1999. H_2O and halogen (F, Cl, Br) behaviour during shallow magma degassing processes. Earth Planet. Sci. Lett. 168, 271–286.
Wang, D.H., Chen, Y.C., Li, H.Q., Chen, Z.H., Yu, J.J., Lu, Y.F., Li, J.Y., 2003. Geological and geochemical features of the Furong tin deposit in Hunan and their significance for mineral prospecting. Geol. Bull. China 22, 50–56 (in Chinese with English abstract).
Wang, D.H., Li, H.Q., Qin, Y., Mei, Y.P., Chen, Z.H., Qu, W.J., Wang, Y.B., Cai, H., Gong, S.Q., He, X.P., 2009. Rock-forming and ore-forming ages of the Yaogangxian tungsten deposit of Hunan Province). Rock Mineral Analysis 28, 201–208 (in Chinese with English abstract).
Wang, D.H., Li, C., Chen, Z.H., Wang, C.H., Huang, F., Qu, W.J., 2012. New application of molybdenite in the study on ore deposits: rare earth elements geochemistry. J. Jilin Univ. (Earth Sci.) 42, 1647–1655 (in Chinese with English abstract).
Wang, X., Griffin, W.L., O'Reilly, S.Y., Li, W.X., 2007. Three stages of zircon growth in magmatic rocks from the Pingtan Complex, eastern China. Acta Geological Sinica (English Edition) 81, 68–80.
Wang, X., Griffin, W.L., Chen, J., 2010. Hf contents and Zr/Hf ratios in granitic zircons. Geochem. J. 44, 65–72.
Wang, X., Griffin, W.L., Chen, J., Huang, P.Y., Li, X., 2011a. U and Th contents and Th/U ratios of zircon in felsic and mafic magmatic rocks: Improved zircon–melt distribution coefficients. Acta Geological Sinica (English Edition) 85, 164–174.
Wang, X., Chen, J., Griffin, W.L., O'Reilly, S.Y., Huang, P.Y., Li, X., 2011b. Two stages of zircon crystallization in the Jingshan monzogranite, Bengbu Uplift: implications for the syn-collisional granites of the Dabie-Sulu UHP orogenic belt and the climax of movement on the Tan–Lu fault. Lithos 122, 201–213.
Wang, Y.L., Pei, R.F., Li, J.W., Qu, W.J., Li, L., Wang, H.L., Du, A.D., 2008. Re–Os dating of molybdenite from the Yaogangxian tungsten deposit, south China, and its geological significance. Acta Geologica Sinica 82, 820–825.
Wang, Y.L., 2008. Tectonic-magma-mineralization of the W–Sn–polymetallic ore concentration area in southern Hunan Province. Ph.D. thesis, Chinese Academy of Geological Sciences, 1–129 (in Chinese with English abstract).
Webster, J.D., De Vivo, B., 2002. Experimental and modeled solubilities of chlorine in aluminosilicate melts, consequences of magma evolution, and implications for exsolution of hydrous chloride melt at Mt. Somma-Vesuvius. Am. Mineralogist 87, 1046–1061.
Wedepohl, K.H., 1995. The composition of the continental crust. Geochimica et Cosmochimica Acta 59, 1217–1232.
Wu, F.Y., Sun, D.Y., Zhang, G.Q., Ren, X.W., 2000. Deep geodynamics of Yanshanian movement. Geol. J. China Univ. 6, 379–388 (in Chinese with English abstract).
Wu, G.Y., Hou, Z.Q., Xiao, Q.H., Wang, T., Yan, Q.R., Chen, H.M., Ma, T.Q., 2008. REE geochemistry and petrogenesis and mineralization of the Yanshanian mineralized granites in the southern Hunan polymetallic ore-concentration region. Geol. China 35, 410–420 (in Chinese with English abstract).
Xie, L., Wang, R.C., Zhu, J.C., Lu, J.J., Zhang, W.L., Che, X.D., Zhang, R.Q., Huang, F.F., 2013. Felsic dykes in the metallogenic area of southern Hunan Province and their implications for mineralization and exploration. Acta Petrologica Sinica 29, 4261–4280 (in Chinese with English abstract).
Xu, J.X., Zeng, Z.L., Wang, D.H., Chen, Z.H., Liu, S.B., Wang, C.H., Ying, L.J., 2008. A new type of tungsten deposit in Southern Jiangxi and the new model of "Five floors

+basement" for prospecting. Acta Geological Sinica 82, 880–887 (in Chinese with English abstract).
Yenes, M., Alvarez, F., Gutierrez-Alonso, G., 1999. Granite emplacement in orogenic compressional conditions: the La Alberca-Bejar granitic area (Spanish Central System, Variscan Iberian Belt). J. Struct. Geol. 21, 1419–1440.
Zhang, Q., 2012. Could granitic magmas experience fractionation and evolution? Acta Petrologica et Mineralogica 31, 252–260 (in Chinese with English abstract).
Zhao, W.W., Zhou, M.F., Chen, W.T., 2016. Growth of hydrothermal baddeleyite and zircon in different stages of skarnization. Am. Mineral. 101, 2689–2700.
Zhao, W.W., Zhou, M.F., Li, Y.H.M., Zhao, Z., Gao, J.F., 2017. Genetic types, mineralization styles, and geodynamic settings of Mesozoic tungsten deposits in South China. J. Asian Earth Sci. 137, 109–140.